IEEE Access
Multidisciplinary ⋮ Rapid Review ⋮ Open Access Journal

Received 31 May 2022, accepted 29 June 2022, date of publication 4 July 2022, date of current version 11 July 2022.

*Digital Object Identifier 10.1109/ACCESS.2022.3188002*

RESEARCH ARTICLE

# Close-Loop Current Control With Current-Sensing Resistor for Electromagnet Driven by Full-Bridge PWM Inverter

**JIN CHENG[1], ZEYI ZHANG[1], AND LEI CHEN[2,3]**

[1]School of Electrical Engineering and Automation, Jiangxi University of Science and Technology, Ganzhou 341000, China
[2]School of Mechanical and Electronic Engineering, Jiangxi College of Applied Technology, Ganzhou 341000, China
[3]Longsheng Intelligent Equipment Company Ltd., Dongguan 523799, China

Corresponding author: Zeyi Zhang (zhangzy@jxust.edu.cn)

This work was supported in part by the Science and Technology Research Project of Educational Department in Jiangxi Province under Grant GJJ210804, in part by the Innovation and Entrepreneurship Training Program for College Students in Jiangxi Province under Grant 202110407015, and in part by the High-Level Talents Research Start-Up Project of Jiangxi University of Science and Technology under Grant 205200100476.

**ABSTRACT** The full-bridge pulse-width-modulation (PWM) inverter is wildly applied to drive the electromagnet and enables advanced technologies, such as the active magnetic bearing (AMB) and the permanent-electro magnetic suspension (PEMS). However, the characteristic relationship between the current through the electromagnet and the duty cycle of the PWM signal has strong nonlinearity around the zero current. Moreover, the electromagnet possesses the induction that results in the time constant and significantly hinders the change of the current. Hence, the open-loop control of the full-bridge PWM inverter cannot accurately or timely tune the current through the electromagnet, especially around the zero current. This work proposes a closed-loop current control approach by three steps: (1) inserting a current-sensing resistor into the middle of the electromagnet, (2) obtaining the current signal with an analog signal-processing circuit, and (3) generating the PWM signal with the bang-bang control circuit. The proposed approach innovatively arranges the current-sensing resistor to take advantage of the symmetry and to minimize the influence from the high-frequency switching of the inverter, so that the measured current signal is comparable to the hall-effect current sensor. The experimental results demonstrate the effectiveness and efficiency of the proposed closed-loop current control approach, though the weak charging capability of the full-bridge PWM inverter still hinders its performance.

**INDEX TERMS** Electromagnetics, DC-DC power converters, bang-bang control.

## I. INTRODUCTION

The full-bridge pulse-width-modulation (PWM) inverter is wildly applied to drive the electromagnet and enables advanced technologies, such as the active magnetic bearing (AMB) [1] and the permanent-electro magnetic suspension (PEMS) [2]. AMB is famous for no contact and eliminates unwanted friction and lubrication so that AMB significantly promotes the high-speed rotating machinery [3]. Moreover, PEMS takes advantage of the Nd-Fe-B permanent magnet to reduce the power consumption of the electromagnet and enables the zero-power suspension [4]. Ren and *et al.* [5] achieved fast and stable levitation of an AMB rotor by compensating for system uncertainties via proper design of interval type-2 membership functions. Zhu and Liu [6] proposed a rotor displacement self-sensing modeling and achieved a six-pole radial hybrid magnetic bearing (HMB). Yalcin and *et al.* [7] applied the PEMS technology for the 3-DoF micro vibration isolation with the zero-power feature.

The current through the electromagnet plays an important role [8] in the robustness of AMB [9] and PEMS [4], [8]. However, the electromagnet possesses a large inductance that leads to the large time constant; besides, the tiny turn-off delay of the full-bridge PWM inverter results in the nonlinear

The associate editor coordinating the review of this manuscript and approving it for publication was Vitor Monteiro.

current-duty cycle characteristic around the zero current [10]. Both the large time constant and the current-duty cycle nonlinearity challenge the timely and accurate control on the current through the electromagnet [11].

In order to achieve the timely and accurate control on the current through the electromagnet, various closed-loop current control approaches are proposed and mainly differ in current sensors / estimations:

- *Hall-effect current sensor* [7], [11]–[15]: prone to electromagnetic disturbance, especially for small current;
- *Resistive current sensor* [9], [16]: prone to fluctuation by the frequent PWM switching;
- *Polynomial estimation* [17]: based on the nonlinear relationship between the current and the PWM duty cycle; inaccurate due to temperature change of the electromagnet; untimely due to the inductance of the electromagnet;
- *State observer* [11]: prone to nonlinearity and highly relies on the dynamic model.

Hence, the hall-effect current sensor and the resistive current sensor can measure the current on the real-time basis, while the polynomial estimation and the state observer suffers from the nonlinear dynamics. Moreover, the resistive current sensor would prevail over the hall-effect current sensor in applications of PEMS and AMB under the small-current condition as a result of the excessive electromagnet disturbance.

Besides, closed-loop current control approaches also differ in control algorithms:

- *Digital one-cycle control (D-OCC)* [18]: it requires a sampling rate as high as the PWM frequency and a high-speed digital signal processing (DSP) controller;
- *Digital model predictive control (D-MPC)* [16]: it requires a high sampling rate and a powerful processor.
- *Bang-bang control (also known as switching control)* [19]: it reaches the target current with a minimized time according to the time constant of the electromagnet.

Hence, in order to optimize the close-loop current control, it generally requires a high sampling rate of the digital controller to capture the current dynamics. On the contrary, the bang-bang control is simple (*without control parameter*) and robust (*fast response*) to work with the electromagnet.

Taking the above literatures into consideration, the present work aims to propose a close-loop current control approach with a current-sensing resistor for the electromagnet driven by the full-bridge PWM inverter. The approach innovatively inserts a current-sensing resistor into the middle of the electromagnet and utilizes the symmetry to minimize the influence from the high-frequency switching of the inverter at the 10 kHz PWM frequency. Moreover, the analog signal-processing circuit amplifies the current signal, whereas the differential comparator realizes the bang-bang control. Furthermore, the resistor-capacitor (RC) filter tunes the bandwidth of the control signal, and the PWM signal is generated based on the sawtooth carrier produced by a timer.

This work is organized as the following. Sec. II is devoted to formulate the theoretical basis for the proposed close-loop current control approach, including the full-bridge inverter, the signal-processing circuit, the bang-bang controller and the stability analysis. In Sec. III, five experiments are carefully demonstrated and discussed to evaluate the performance of the proposed approach. In particular, Exp. 1 illustrates the high-frequency ripples on the current signal due to the frequent switching of the inverter at the 10 kHz PWM frequency; Exp. 2 shows the current-duty cycle nonlinearity and the accuracy of the measured current signal; Exps. 3, 4, and 5 verify the proposed approach under various current setpoints. Last but not least, concluding remarks are addressed in Sec. IV.

## II. THEORETICAL MODELLING

### A. FULL-BRIDGE INVERTER

As reported in the previous work [10], Fig. 1 shows the circuit of the L298N full-bridge PWM inverter that is controlled by the PWM signal. In particular, the current-sensing resistor, $R_{curr}$, is serially connected into the middle of the electromagnet, which consists of two inductors and two resistors, i.e., $L_{left}$, $L_{right}$, $R_{left}$, and $R_{right}$. In order to minimize the influence from the inserted current-sensing resistor on the electromagnet, $R_{curr}$ is much smaller than $R_{left}$ and $R_{right}$. Denote the voltage across $R_{curr}$ as $u_{MN}$ and the current through $R_{curr}$ as $i_{MN}$, so that we can write,

$$u_{MN} = U_M - U_N = R_{curr} i_{MN}, \tag{1}$$

where $U_M$ and $U_N$ are two node voltages of $R_{curr}$.

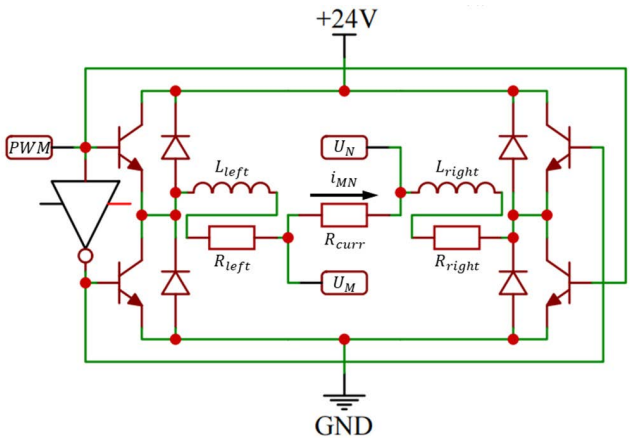


**FIGURE 1.** Circuit of L298N full-bridge PWM inverter. The current-sensing resistor, $R_{curr}$, is serially connected into the middle of the electromagnet that consists of $L_{left}$, $L_{right}$, $R_{left}$, and $R_{right}$. $U_M$ and $U_N$ are two node voltages of $R_{curr}$. The NOT gate is used to reverse the PWM signal.

Moreover, the electromagnet and $R_{curr}$ are driven by L298N. Denote the voltage output from L298N as $u$, and we can write the differential equation,

$$u = R_{total} i_{MN} + L_{total} di_{MN}/dt, \tag{2}$$

where $R_{total} = R_{left} + R_{curr} + R_{right}$ and $L_{total} = L_{left} + L_{right}$. Equation (2) indicates a first-order self-balance process with the time constant of $\tau = L_{total}/R_{total}$.

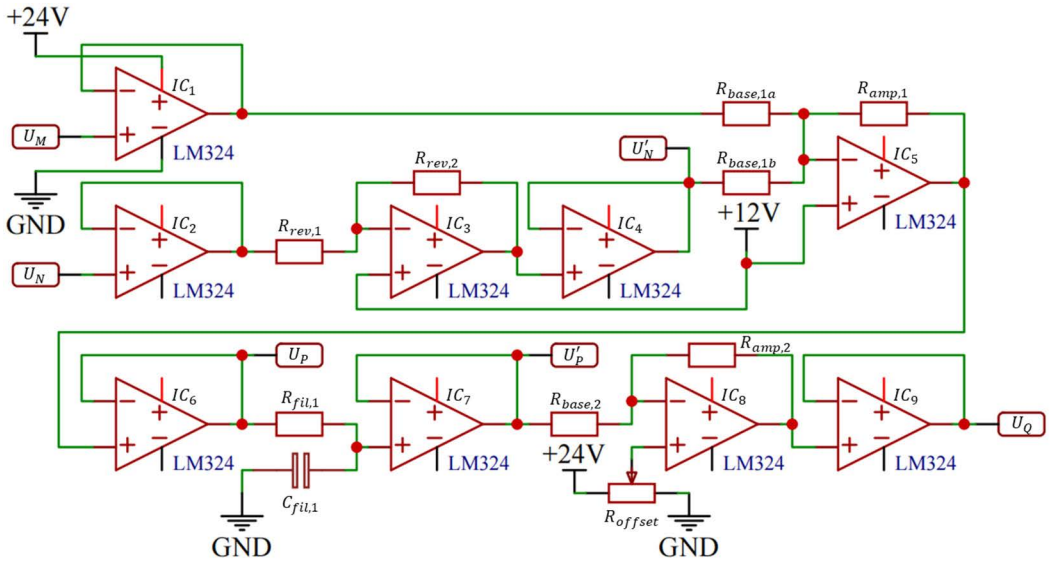


**FIGURE 2.** The signal-processing circuit to convert the two node voltages, $U_M$ and $U_N$, into the current signal, $U_Q$. $U'_N$, $U_P$, and $U'_P$ are three intermediate voltages. All LM324 work at 24 V power supply.

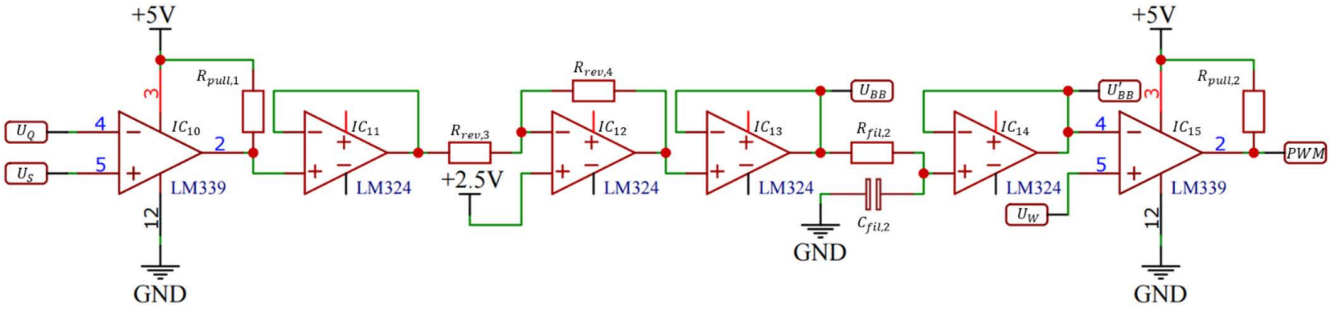


**FIGURE 3.** The bang-bang control circuit to generate the PWM signal. $U_Q$ is the current signal, $U_S$ is the current setpoint, and $U_W$ is the sawtooth carrier. $U_{BB}$ and $U'_{BB}$ are two intermediate voltages. The first differential comparator, $IC_{10}$, realizes the bang-bang control, whereas the second one, $IC_{15}$, generates the PWM signal. All LM339 and LM324 work at 5 V power supply.

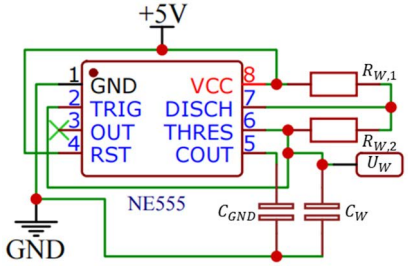


**FIGURE 4.** The astable circuit of NE555 to generate the sawtooth carrier, $U_W$.

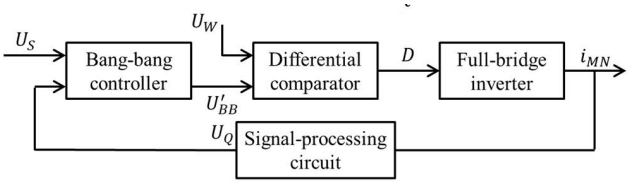


**FIGURE 5.** The block diagram of the proposed close-loop current control approach for the electromagnet with the full-bridge PWM inverter.

Furthermore, $u$ is controlled by the PWM signal as,

$$u \approx \begin{cases} +U, & \text{PWM} = \text{HIGH} \\ -U, & \text{PWM} = \text{LOW}, \end{cases} \tag{3}$$

where $U = 24$ V denotes the power supply voltage.

Equation (3) indicates that $U_M$ and $U_N$ may potentially fluctuate between 0 V and $U$ if $R_{left} = 0$ or $R_{right} = 0$ [10].

In order to minimize the voltage fluctuation of $U_M$ and $U_N$, the electromagnet is separated into two equal halves, i.e., $R_{left} = R_{right} \gg R_{curr}$ and $L_{left} = L_{right}$, so that we can derive $U_M$ and $U_N$ by symmetry,

$$\begin{cases} U_M = (U + R_{curr} i_{MN}) / 2 \\ U_N = (U - R_{curr} i_{MN}) / 2, \end{cases} \tag{4}$$

which minimizes the influence from the high-frequency switching of the inverter as a result of small $R_{curr}$.

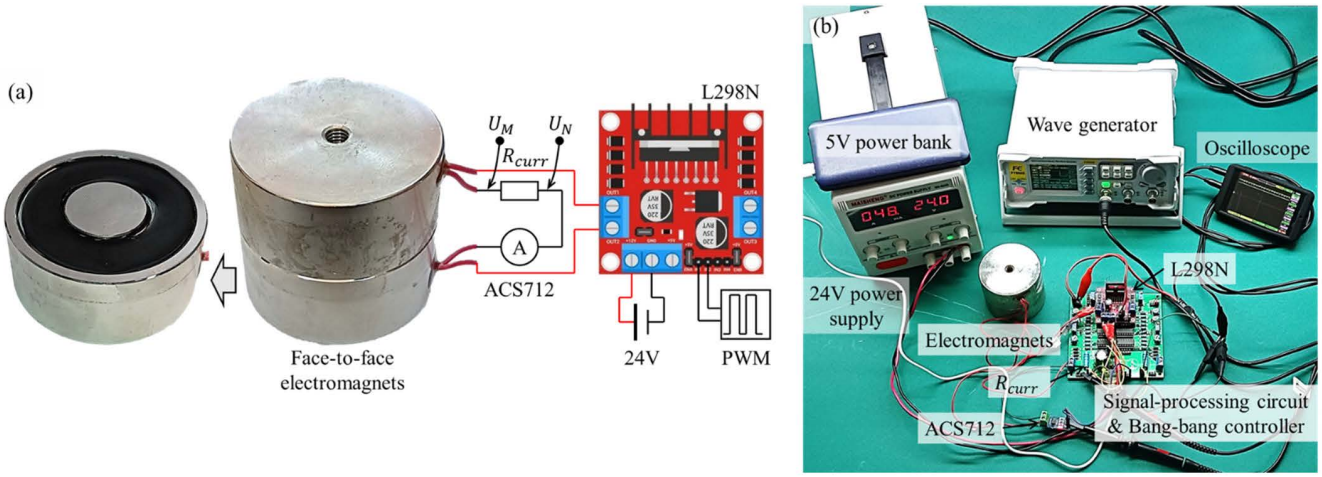


**FIGURE 6.** Experiment setup of the close-loop current control for the electromagnet driven by the L298N full-bridge PWM inverter, (a) graphic diagram, and (b) photograph. Two equivalent electromagnets are face-to-face stacked, and the current-sensing resistor as well as the ACS712 hall-effect current sensor are serially connected into the two electromagnets. $U_M$ and $U_N$ are connected to the signal-processing circuit, whereas the PWM signal is generated by the bang-bang control circuit or the wave generator. The oscilloscope is used to capture the raw data.

### B. SIGNAL-PROCESSING CIRCUIT

Fig. 2 shows the signal-processing circuit to convert the two node voltages, $U_M$ and $U_N$, into the current signal, $U_Q$. $IC_i$ ($i = 1, 2, \ldots, 9$) are nine LM324 operational amplifiers and work at 24 V power supply. In particular, $IC_1$, $IC_2$, $IC_4$, $IC_6$, $IC_7$, and $IC_9$ serve as the voltage followers, whereas $IC_3$, $IC_5$, and $IC_8$ aim to process signals as detailed below.

$IC_3$ reverses $U_N$ as,

$$U'_N = U - U_N, \tag{5}$$

where $R_{rev,1} = R_{rev,2}$.

$IC_5$ subtracts $U_N$ from $U_M$ as,

$$\frac{U_M - U/2}{R_{base,1a}} + \frac{U'_N - U/2}{R_{base,1b}} = \frac{U/2 - U_P}{R_{amp,1}}, \tag{6}$$

where $R_{base,1a} = R_{base,1}$. Solving (6) with (5) gives,

$$U_P = U/2 - \frac{R_{amp,1}}{R_{base,1a}} u_{MN}. \tag{7}$$

The 1st RC filter consisting of $R_{fil,1}$ and $C_{fil,1}$ removes high-frequency ripples [20] on $U_P$ with the cutoff frequency at $f_{fil,1} = 1/2\pi R_{fil,1} C_{fil,1}$ and outputs $U'_P$ ($\approx U_P$), which is to be further illustrated in Sec. III(B).

$IC_8$ further shifts and amplifies $U'_P$ as,

$$\frac{U'_P - U_{offset}}{R_{base,2}} = \frac{U_{offset} - U_Q}{R_{amp,2}}, \tag{8}$$

where $U_{offset}$ is tuned by the potentiometer $R_{offset}$. Solving (8) with (1) and (7) gives,

$$\begin{aligned} U_Q &= \left(1 + \frac{R_{amp,2}}{R_{base,2}}\right) U_{offset} - \frac{R_{amp,2}}{R_{base,2}} U'_P \\ &\approx \frac{R_{amp,1}}{R_{base,1a}} \frac{R_{amp,2}}{R_{base,2}} R_{curr} i_{MN} + \left(1 + \frac{R_{amp,2}}{R_{base,2}}\right) U_{offset} \\ &\quad - \frac{R_{amp,2}}{2R_{base,2}} U. \end{aligned} \tag{9}$$

**TABLE 1.** Physical properties.

| Symbol | Quantity | Value | Unit |
|---|---|---|---|
| $R_{total}$ | Total resistance | 27.0 | Ω |
| $R_{curr}$ | Current-sensing resistance | 0.1 | Ω |
| $L_{total}$ | Total inductance | 334.1 | mH |
| $\tau$ | time constant | 12.4 | ms |
| $U$ | Power supply voltage | 24 | V |
| $C_W$, $C_{GND}$ | Waveform capacitances | 10 | nF |
| $R_{W,1}$ | Waveform resistance | 630 | Ω |
| $R_{W,2}$ | Waveform resistance | 6.88 | kΩ |
| $f_{\mathrm{PWM}}$ | PWM frequency | 10 | kHz |
| $D$ | PWM duty cycle | 0.0 to 1.0 | - |
| $R_{rev,1}$, $R_{rev,2}$, $R_{rev,3}$, $R_{rev,4}$ | Resistances to reverse signals | 100 | kΩ |
| $R_{base,1a}$, $R_{base,1b}$ | Resistances as the base | 220 | kΩ |
| $R_{amp,1}$ | Resistance to amplify signal | 1 | MΩ |
| $R_{base,2}$ | Resistance as the base | 20 | kΩ |
| $R_{amp,2}$ | Resistance to amplify signal | 41.2 | kΩ |
| $U_{offset}$ | Offset voltage | 8.62 | V |
| $R_{fil,1}$ | Resistance of 1st RC filter | 160 | kΩ |
| $R_{fil,2}$ | Resistance of 2nd RC filter | 480 | kΩ |
| $C_{fil,1}$, $C_{fil,2}$ | Capacitances of RC filters | 1 | nF |
| $f_{fil,1}$ | Cutoff frequency of 1st RC filter | 1.0 | kHz |
| $f_{fil,2}$ | Cutoff frequency of 2nd RC filter | 0.33 | kHz |
| $R_{pull,1}$, $R_{pull,2}$ | Pull-up resistances | 5 | kΩ |
| $U_P$ | Raw signal | ≈ 12.5 | V |
| $U_Q$ | Current signal | 0.9 to 2.5 | V |
| $U'_{BB}$ | Signal from bang-bang control circuit | 1.4 to 3.6 | V |

Hence, when $i_{MN} = 0$ (i.e., no current through the electromagnet), $U_Q = \left(1 + \frac{R_{amp,2}}{R_{base,2}}\right) U_{offset} - \frac{R_{amp,2}}{2R_{base,2}} U$. Besides, the gain between $i_{MN}$ and $U_Q$ is $\frac{R_{amp,1}}{R_{base,1a}} \frac{R_{amp,2}}{R_{base,2}} R_{curr}$.

### C. BANG-BANG CONTROLLER

Fig. 3 shows the bang-bang control circuit to generate the PWM signal. $IC_{10}$ and $IC_{15}$ are two LM339 differential comparators and $IC_i$ ($i = 11, 12, 13, 14$) are four LM324

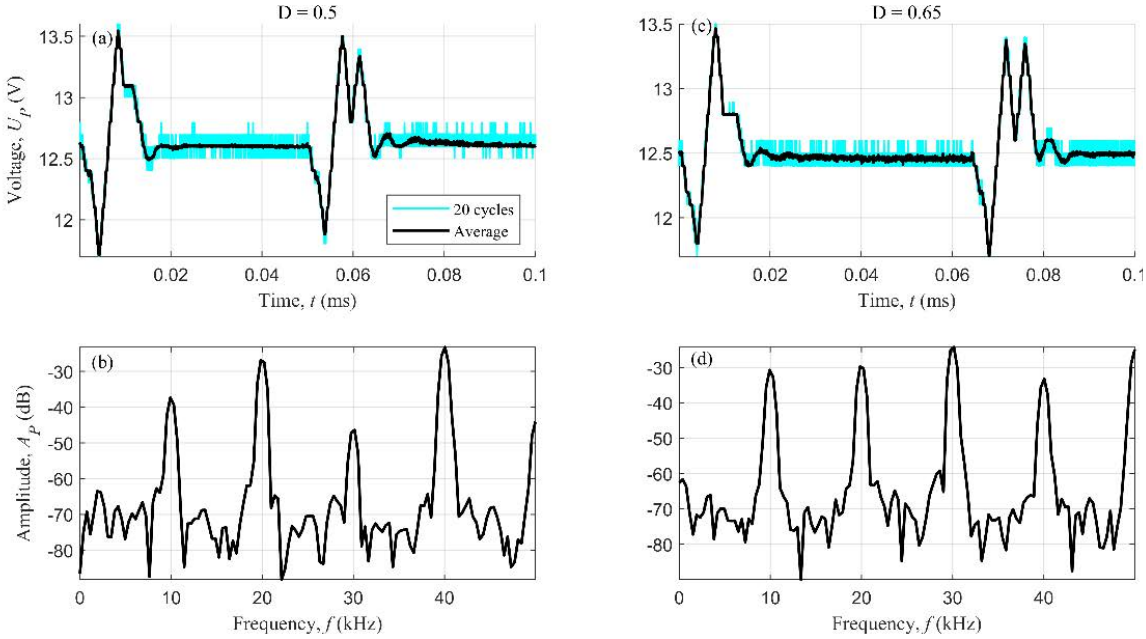


**FIGURE 7.** Ripples on the raw signal with two duty cycles, $D = 0.5$ and 0.65, (a & c) $U_P$, and (b & d) fast Fourier transformation (FFT) of $U_P$. The cyan curves in (a & c) are the raw data out of 20 consecutive cycles, whereas the black curves are the corresponding averaged values. The sampling rate is 25 MHz.

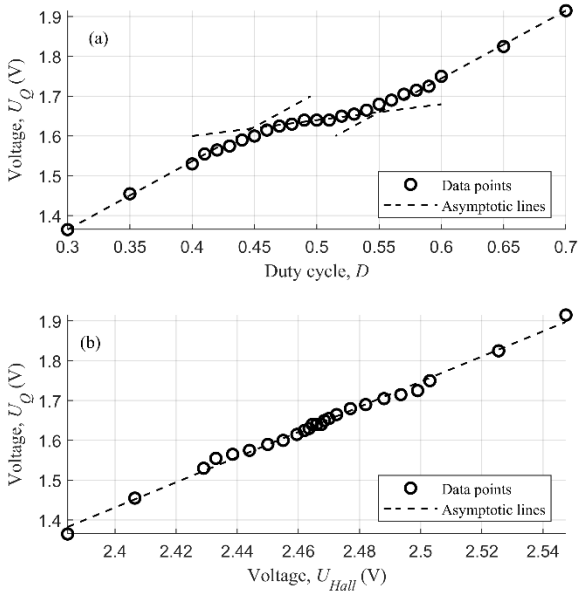


**FIGURE 8.** (a) Nonlinear relationship between the current signal and the duty cycle, with three asymptotic lines drawn to highlight the nonlinearity, (b) linear relationship between the current signal and the hall-effect signal, with one asymptotic line.

operational amplifiers. All LM339 and LM324 work at 5 V power supply. In particular, $IC_{11}$, $IC_{13}$, and $IC_{14}$ serve as the voltage followers, $IC_{10}$ realizes the bang-bang control, $IC_{12}$ reverses the control signal, and $IC_{15}$ generates the PWM signal, as detailed below.

Since $R_{rev,3} = R_{rev,4}$, the bang-bang control signal, $U_{BB}$, can be expressed as,

$$U_{BB} = \begin{cases} \text{HIGH}, & U_Q > U_S \\ \text{LOW}, & U_Q < U_S, \end{cases} \tag{10}$$

where $U_S$ is the current setpoint.

Moreover, the 2nd RC filter consisting of $R_{fil,2}$ and $C_{fil,2}$ removes high-frequency noises from $U_{BB}$ with the cutoff frequency at $f_{fil,2} = 1/2\pi R_{fil,2}C_{fil,2}$ and outputs $U'_{BB}$ ($\approx U_{BB}$). Technically, in order to maintain a sufficient bandwidth of the bang-bang control circuit, $f_{fil,1}$ should be larger than $f_{fil,2}$ but smaller than the PWM frequency, $f_{\text{PWM}}$, i.e., $f_{fil,2} < f_{fil,1} < f_{\text{PWM}}$.

Furthermore, $U_W$ is the sawtooth carrier generated by the NE555 timer under the astable operation in Fig. 4 and fluctuates between 1.65 V and 3.3 V. By referring to the datasheet of NE555, the frequency of the astable waveform is,

$$f_{\text{PWM}} = 1.44/\left(R_{W,1} + 2R_{W,2}\right) C_W. \tag{11}$$

Nevertheless, $IC_{15}$ generates the PWM signal by comparing $U'_{BB}$ and $U_W$ as,

$$\text{PWM} = \begin{cases} \text{HIGH}, & U_W > U'_{BB} \\ \text{LOW}, & U_W < U'_{BB}. \end{cases} \tag{12}$$

which indicates that the duty cycle, $D$, increases as the decrease of $U'_{BB}$.

### D. STABILITY ANALYSIS

Fig. 5 shows the block diagram of the proposed close-loop current control approach for electromagnet with L298N.

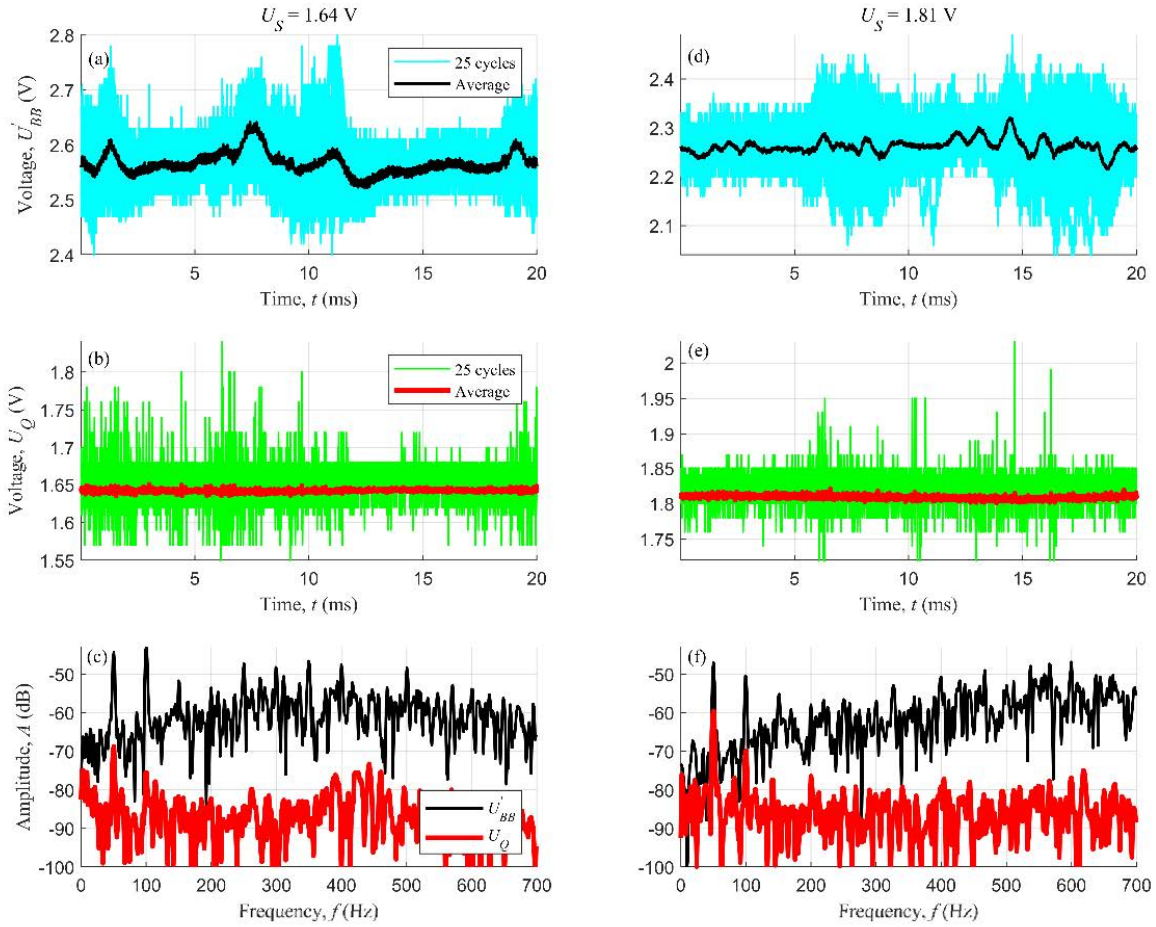


**FIGURE 9.** Close-loop current control for two current setpoints, $U_S = 1.64$ V and 1.81 V, (a & d) dynamic responses of $U'_{BB}$, (b & e) dynamic responses of $U_Q$, and (c & f) FFT of $U'_{BB}$ and $U_Q$. The cyan curves in (a & d) are the raw data out of 25 consecutive cycles, whereas the black curves are the corresponding averaged values. The green curves in (b & e) are the raw data out of 25 consecutive cycles, whereas the red curves are the corresponding averaged values. The sampling rate is 100 kHz.

In order to analyze its stability, we consider the following two scenarios:

- When the current signal is larger than the associated setpoint, i.e., $U_Q > U_S$, $U'_{BB}$ will increase by (10), $D$ will decrease by (12), $i_{MN}$ will decrease by (3), which results in the decrease of $U_Q$ by (9).
- When the current signal is lower than the associated setpoint, i.e., $U_Q < U_S$, $U'_{BB}$ will decrease by (10), $D$ will increase by (12), $i_{MN}$ will increase by (3), which results in the increase of $U_Q$ by (9).

Therefore, the proposed approach can stabilize the current signal at the associated setpoint, i.e., $U_Q \approx U_S$.

In addition, this work considers a low-voltage scenario (24 V), whereas a high-voltage counterpart (200∼600 V) might differ in the selection of the full-bridge PWM inverter in Fig. 1 as well as those operational amplifiers in Fig. 2 to meet the high-voltage requirement.

## III. RESULTS AND DISCUSSION

### A. EXPERIMENT SETUP

In order to verify the proposed close-loop current control approach, Fig. 6(a) shows the graphic experiment setup consisting of two face-to-face-stacked electromagnets, the current-sensing resistor, the L298N full-bridge PWM inverter, and the ACS712 hall-effect current sensor (*with the optimized accuracy range from −5 A to +5 A, the sensitivity around 185 mV/A and the bandwidth at 50 kHz*). Besides, Fig. 6(b) shows the photograph which further shows the 5 V power bank, the 24 V power supply, the wave generator, the oscilloscope, the signal-processing circuit, and the bang-bang control circuit. The current-sensing resistor is serially connected into the two electromagnets, $U_M$ and $U_N$ are connected to the signal-processing circuit, and its measured current signal is to be compared with that measured by the ACS712 hall-effect current sensor. The PWM signal is generated by the bang-bang control circuit or the wave

generator. The oscilloscope is used to capture the raw data. Also, physical properties regarding the experiment setup are listed in Table 1.

In particular, $R_{base,1a}$, $R_{amp,1}$, $R_{base,2}$, $R_{amp,2}$, and $U_{offset}$ are carefully tuned to meet the following three conditions,

$$\begin{cases} U_Q(D=0.5) = \left(1+\dfrac{R_{amp,2}}{R_{base,2}}\right)U_{offset} = \dfrac{R_{amp,2}}{2R_{base,2}}U = 1.65\,\text{V} \\ U_Q(D=1) - U_Q(D=0) = 2\dfrac{R_{amp,1}}{R_{base,1a}}\dfrac{R_{amp,2}}{R_{base,2}}R_{curr}|i_{MN}|_{max} = 1.65\,\text{V}, \\ \Delta U_Q/\Delta i_{MN} = \dfrac{R_{amp,1}}{R_{base,1a}}\dfrac{R_{amp,2}}{R_{base,2}}R_{curr} = 0.93\,\text{V/A} \end{cases} \quad (13)$$

where $i_{MN}\,(D=0.5) = 0$ A and $|i_{MN}|_{max} = U/R_{total}$.

Moreover, $R_{W,2}$ is tuned to realize $f_{\text{PWM}} = 10$ kHz according to (11).

### B. EXP. 1: RIPPLES ON $U_P$

Since $f_{\text{PWM}} = 10$ kHz, the high-frequency switching of L298N results in ripples on $U_P$ [10, 20]. Fig. 7 shows two sets of data with $D = 0.5$ and 0.65. We observe that ripples tightly correspond to both switch-on and -off of L298N and have frequencies at 10 kHz together with higher harmonic frequencies. Besides, the amplitude of the ripples is less than 1 V and is less than 5% of the 24 V power supply voltage, which agrees well with (4) to minimize the influence from the high-frequency switching of the inverter.

Moreover, in order to remove the high-frequency ripples on $U_P$, the 1st RC filter is applied in the signal-processing circuit in Fig. 2. From Table I, $R_{fil,1} = 160$ kΩ and $C_{fil,1} = 1$ nF lead to the cutoff frequency at $f_{fil,1} = 1.0$ kHz that is sufficient.

### C. EXP. 2: CURRENT SIGNAL $U_Q$

By applying the PWM signal with various duty cycles to the full-bridge PWM inverter, the signal-processing circuit outputs the current signal ($U_Q$) that is to be compared with the hall-effect signal ($U_{hall}$) measured by the ACS712 hall-effect current sensor.

Fig. 8(a) shows the nonlinear relationship between the current signal and the duty cycle [10]. In particular, three asymptotic lines with the slopes of around 1.72, 0.40, and 1.70 from left to right are drawn to highlight the nonlinearity. In other words, the sensitivity of $U_Q$ with respect to $D$ significantly drops for more than 75% when approaching to $D = 0.5$ where the corresponding current through the electromagnet is zero. Therefore, the nonlinearity makes it inaccurate to control the small current through the electromagnet by an open-loop control on the duty cycle.

Fig. 8(b) shows the linear relationship between the current signal and the hall-effect signal, which can be well represented by the asymptotic line, $U_Q = 3.16U_{hall} - 6.15$, with a high coefficient of determination, $R^2 = 0.9932$. Therefore, the proposed signal-processing circuit demonstrates a sufficient accuracy that is comparable to the ACS712 hall-effect current sensor.

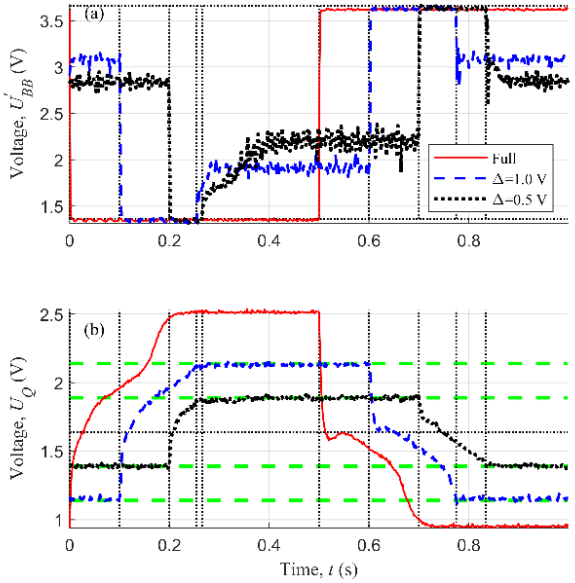


**FIGURE 10.** Close-loop current control for step-change $U_S$ under three scenarios, (a) $U'_{BB}$ and (b) $U_Q$. The curves are the averaged values for 11 consecutive cycles, whereas the sampling rate is 625 Hz. The step-change frequency is 1 Hz, whereas the step changes occur at $t = 0.0$ and 0.5 s, $t = 0.1$ and 0.6 s, and $t = 0.2$ and 0.7 s for red solid, blue dashed, and black dotted curves, respectively. The step changes are 3.3 V, 1.0 V, and 0.5 V for red solid, blue dashed, and black dotted curves, respectively, whereas the mean value of step-change $U_S$ is 1.64 V. The two horizontal black dotted lines in (a) correspond to the upper and lower saturations of $U'_{BB}$. The four horizontal green dashed lines in (b) correspond to 1.14 V, 1.39 V, 1.89 V, and 2.14 V, respectively, whereas the vertical black dotted lines correspond to the saturations of $U'_{BB}$ in (a).

### D. EXP. 3: CONSTANT $U_S$

Fig. 9 shows the close-loop current control for two constant setpoints, $U_S = 1.64$ V and 1.81 V. In Figs. 9(a & d), we observe that the control signal ($U'_{BB}$) has rigorous high-frequency noise due to the bang-bang control in (10). In order to remove the high-frequency noise on $U_{BB}$, the 2nd RC filter is applied in the bang-bang control circuit in Fig. 3. From Table I, $R_{fil,2} = 480$kΩ and $C_{fil,2} = 1$ nF lead to the cutoff frequency at $f_{fil,2} = 0.33$ kHz that is sufficient.

Moreover, in Figs. 9(c & f), we observe that noises on the current signal ($U_Q$) are significantly smaller (around 20 dB) than those on the control signal ($U'_{BB}$). In particular, the 50 Hz fluctuations in Figs. 9(c & f) result from the 220 V AC power supply for the 24 V DC power supply. Hence, 20 ms is determined as the time span of Figs. 9(a, b, d & e).

Furthermore, though slight noises are observed on $U_Q$ in Figs. 9(b & e), the averaged $U_Q$ are much more stable than the averaged $U'_{BB}$ in Figs. 9(a & d). Therefore, the proposed close-loop current control approach can stabilize $U_Q$ at the constant setpoint and compensate the external noise by adjusting $U'_{BB}$.

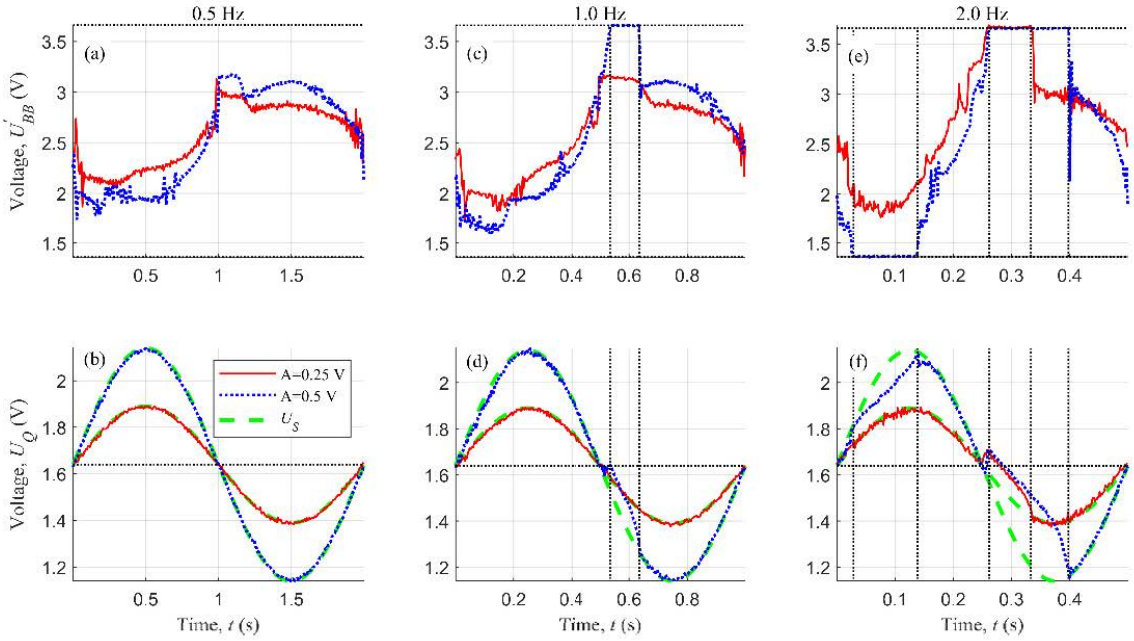


**FIGURE 11.** Close-loop current control for sinusoidal $U_S$ under two amplitudes and three frequencies, (a, c & e) $U'_{BB}$ and (b, d &f) $U_Q$. The curves are the averaged values for 11 consecutive cycles, whereas the sampling rates are 156.25 Hz, 312.5 Hz, and 625 Hz for 0.5 Hz, 1.0 Hz, and 2.0 Hz sinusoidal frequencies, respectively. The sinusoidal amplitudes are 0.25 V and 0.5 V for red solid and blue dotted curves, respectively, whereas the green dashed curves illustrate sinusoidal $U_S$. The mean value of sinusoidal $U_S$ is 1.64 V. The two horizontal black dotted lines in (a, c e) corresponds to the upper and lower saturations of $U'_{BB}$, whereas the vertical black dotted lines correspond to the saturations of $U'_{BB}$ in (a, c e).

### E. EXP. 4: STEP-CHANGE $U_S$

Fig. 10 shows the close-loop current control for step-change $U_S$ under three scenarios. In Fig. 10(a), we observe that the step change in $U_S$ results in the saturation of $U'_{BB}$ according to the bang-bang control. Moreover, the saturation duration of $U'_{BB}$ increases as the increase of the step change. Furthermore, $U_Q$ is already close to respective $U_S$ in Fig. 10(b) when $U'_{BB}$ leaves its upper or lower saturations in Fig. 10(a). Therefore, the proposed close-loop current control approach can make full use of the bang-bang control without sacrificing the accuracy.

Besides, since $U_Q = 1.64$ V corresponds to $D \approx 0.5$ ($i_{MN} \approx 0$) in Fig. 2, Fig. 10(b) also indicates that the discharging capability of the full-bridge PWM inverter, i.e., $|i_{MN}|$ decreases, is much stronger than its charging capability, i.e.,$|i_{MN}|$ increases. In other words, the weak charging capability significantly hinders the proposed close-loop current control approach.

### F. EXP. 5: SINUSOIDAL $U_S$

Fig. 11 shows the close-loop current control for sinusoidal $U_S$ under two amplitudes and three frequencies. We observe that $U_Q$ can faithfully follow $U_S$ for both $A = 0.25$ V and $A = 0.5$ V in Fig. 11(b), while $U'_{BB}$ does not saturate in Fig. 11(a). However, $U_Q$ for $A = 0.5$ V deviates from $U_S$ in Fig. 11(d) while $U'_{BB}$ for $A = 0.5$ V saturates in Fig. 11(c). Similarly, the deviations of $U_Q$ from $U_S$ in Fig. 11(f) and the saturations of $U'_{BB}$ in Fig. 11(e) occur simultaneously. Moreover, the saturations of $U'_{BB}$ in Fig. 11(c & e) take place mainly during the charging of the electromagnet as shown in Fig. 10(b). Therefore, the proposed close-loop current control approach tries to entirely utilize the charging and discharging capabilities to follow the varying current setpoint but is significantly restricted by the weak charging capability of the full-bridge PWM inverter.

## IV. CONCLUSION

This work proposes a close-loop control approach to accurately and timely tune the current through the electromagnet driven by the full-bridge PWM inverter. The proposed approach innovatively inserts a current-sensing resistor into the middle of the electromagnet to minimize the voltage fluctuation and obtain the current signal by an analog signal-processing circuit that is comparable to the hall-effect current sensor. Moreover, the bang-bang controller is realized by the differential comparator to entirely utilize the charging and discharging capabilities of the full-bridge PWM inverter. The experimental results demonstrate that the proposed approach can effectively overcome the current-duty cycle nonlinearity of the full-bridge PWM inverter and faithfully follow the current setpoint. However, the approach is significantly restricted by the weak charging capability of the full-bridge PWM inverter with the electromagnet, which may be addressed by increasing the power supply voltage.

## CONFLICTS OF INTEREST

The authors declare no conflict of interest.

## REFERENCES


[1] H. S. Zad, T. I. Khan, and I. Lazoglu, "Design and adaptive sliding-mode control of hybrid magnetic bearings," (in English), *IEEE Trans. Ind. Electron.*, vol. 65, no. 3, pp. 2537–2547, Mar. 2018, doi: 10.1109/Tie.2017.2739682.

[2] G. Liu, Y. Lu, Y. Liu, Z. Dong, and Z. Ye, "Research on two-dimensional external magnetic drive method of maglev ball based on force imbalance," *Rev. Sci. Instrum.*, vol. 91, no. 10, Oct. 2020, Art. no. 105003, doi: 10.1063/5.0017776.

[3] S.-L. Chen, S.-Y. Lin, and C.-S. Toh, "Adaptive unbalance compensation for a three-pole active magnetic bearing system," (in English), *IEEE Trans. Ind. Electron.*, vol. 67, no. 3, pp. 2097–2106, Mar. 2020, doi: 10.1109/Tie.2019.2903747.

[4] Z. Zhang, T. Gao, Y. Qin, J. Yang, and F. Zhou, "Numerical study for zero-power maglev system inspired by undergraduate project kits," (in English), *IEEE Access*, vol. 8, pp. 90316–90323, 2020, doi: 10.1109/Access.2020.2994128.

[5] G.-P. Ren, Z. Chen, H.-T. Zhang, Y. Wu, H. Meng, D. Wu, and H. Ding, "Design of interval type-2 fuzzy controllers for active magnetic bearing systems," (in English), *IEEE/ASME Trans. Mechatronics*, vol. 25, no. 5, pp. 2449–2459, Oct. 2020, doi: 10.1109/Tmech.2020.2978018.

[6] H. Zhu and T. Liu, "Rotor displacement self-sensing modeling of six-pole radial hybrid magnetic bearing using improved particle swarm optimization support vector machine," (in English), *IEEE Trans. Power Electron.*, vol. 35, no. 11, pp. 12296–12306, Nov. 2020, doi: 10.1109/Tpel.2020.2982746.

[7] B. C. Yalçın and K. Erkan, "3-DoF zero power micro vibration isolation via linear matrix inequalities based on $H_\infty$ and $H_2$ control approaches," (in English), *Mech. Syst. Signal Process.*, vol. 153, May 2021, Art. no. 107506, doi: 10.1016/j.ymssp.2020.107506.

[8] S. Banerjee, M. K. Sarkar, P. K. Biswas, R. Bhaduri, and P. Sarkar, "A review note on different components of simple electromagnetic levitation systems," (in English), *IETE Tech. Rev.*, vol. 28, no. 3, pp. 256–264, May 2011, doi: 10.4103/0256-4602.81241.

[9] Y. Ren and J. Fang, "Current-sensing resistor design to include current derivative in PWM H-bridge unipolar switching power amplifiers for magnetic bearings," *IEEE Trans. Ind. Electron.*, vol. 59, no. 12, pp. 4590–4600, Dec. 2012.

[10] L. Chen, J. Guo, B. Zhu, and Z. Zhang, "Electronic nonlinearity of full-bridge PWM inverter for zero-power PEMS system," *IEEE Access*, vol. 10, pp. 37670–37677, 2022, doi: 10.1109/access.2022.3165307.

[11] K. Oguchi and Y. Tomigashi, "Digital control for a magnetic suspension system as an undergraduate project," *Int. J. Electr. Eng. Educ.*, vol. 27, no. 3, pp. 226–236, Jul. 2016, doi: 10.1177/002072099002700305.

[12] A. E. Hajjaji and M. Ouladsine, "Modeling and nonlinear control of magnetic levitation systems," *IEEE Trans. Ind. Electron.*, vol. 48, no. 4, pp. 831–838, Aug. 2001, doi: 10.1109/41.937416.

[13] S. H. Lee, H. K. Sung, J. T. Lim, and Z. Bien, "Self-tuning control of electromagnetic levitation systems," *Control Eng. Pract.*, vol. 8, no. 7, pp. 749–756, Sep. 2000, doi: 10.1016/S0967-0661(00)00005-8.

[14] S. Banerjee, T. K. S. Kumar, J. Pal, and D. Prasad, "Controller design for large-gap control of electromagnetically levitated system by using an optimization technique," (in English), *IEEE Trans. Control Syst. Technol.*, vol. 16, no. 3, pp. 408–415, May 2008, doi: 10.1109/Tcst.2007.906272.

[15] R.-J. Wai, J.-D. Lee, and K.-L. Chuang, "Real-time PID control strategy for maglev transportation system via particle swarm optimization," (in English), *IEEE Trans. Ind. Electron.*, vol. 58, no. 2, pp. 629–646, Feb. 2011, doi: 10.1109/Tie.2010.2046004.

[16] T. Bächle, S. Hentzelt, and K. Graichen, "Nonlinear model predictive control of a magnetic levitation system," *Control Eng. Pract.*, vol. 21, no. 9, pp. 1250–1258, Sep. 2013, doi: 10.1016/j.conengprac.2013.04.009.

[17] W. Yu and X. O. Li, "A magnetic levitation system for advanced control education," in *Proc. 19th IFAC World Congr.*, Cape Town, South Africa, 2014, pp. 9032–9037, doi: 10.3182/20140824-6-ZA-1003.00147.

[18] Q. L. Jiang, D. Liang, and F. Yan, "Application of digital one-cycle control for current in electromagnetic suspension system," *J. Southwest Jiaotong Univ.*, vol. 54, no. 1, pp. 1–8, 2019.

[19] S. Sivrioglu, "Adaptive backstepping for switching control active magnetic bearing system with vibrating base," (in English), *IET Control Theory Appl.*, vol. 1, no. 4, pp. 1054–1059, Jul. 2007, doi: 10.1049/iet-cta:20050473.

[20] K. M. Smedley and S. Ćuk, "One-cycle control of switching converters," *IEEE Trans. Power Electron.*, vol. 10, no. 6, pp. 625–633, Nov. 1995.


**JIN CHENG** is currently pursuing the bachelor's degree with the Jiangxi University of Science and Technology. His research interests include current sensor and maglev drug delivery systems.

**ZEYI ZHANG** received the bachelor's and Ph.D. degrees from the University of Hong Kong, in 2014 and 2018, respectively. He is currently the Vice Professor with the School of Electrical Engineering and Automation, Jiangxi University of Science and Technology. His research interests include permanent maglev and automatic control.

**LEI CHEN** received the bachelor's degree from Nanchang Hangkong University, in 2010, and the master's degree from the Guangdong University of Technology, in 2013. He is currently a Lecturer with the Jiangxi College of Applied Technology. His research interests include mechanics, electronics, and automatic control.